ACS APPLIED MATERIALS & INTERFACES

Open Access
This article is licensed under CC-BY-NC-ND 4.0

www.acsami.org
Research Article

Interfacial Metal Chlorides as a Tool to Enhance Charge Carrier Dynamics, Electroluminescence, and Overall Efficiency of Organic Optoelectronic Devices

Shabnam Ahadzadeh, Beatriz de la Fuente, Hamid Hamed, Guy Brammertz, Tom Hauffman, Sofie Cambré, Wim Deferme,* and Rachith Shanivarasanthe Nithyananda Kumar

Cite This: ACS Appl. Mater. Interfaces 2024, 16, 65687−65701
Read Online

ACCESS | Metrics & More | Article Recommendations | Supporting Information

ABSTRACT: Interface engineering is the key to optimizing optoelectronic device performance, addressing challenges like reducing potential barriers, passivating interface traps, and controlling recombination of charges. Metal fluorides such as lithium fluoride are employed in interface modification within organic devices due to their strong dipole characteristics but carry health risks, high processing costs, and minimal impact on interface traps in organic electronics. Hence, this study investigates alternative metal chloride (MC) nanocrystals (sodium, cesium, rubidium, and potassium chlorides) that exhibit a strong dipole moment and are readily processable with the aim of reducing the influence of interface traps. Interfacial properties are assessed via various techniques, including electron paramagnetic resonance, X-ray/ultraviolet photoelectron spectroscopy, capacitance−voltage measurements, and density functional theory calculations. In organic light-emitting diodes (OLEDs), the influence of MC on charge transfer, trap density, and light emission properties is evaluated. MCs in ZnO:PEIE nanocomposites (NCs) show improved charge transport, accelerated trapping/detrapping in ZnO:PEIE NCs, and a 50% reduction in active traps in NaCl-based devices versus the reference without MCs. RbCl-, CsCl-, and NaCl-based OLEDs exhibit substantial reductions in the potential barrier between the electron injection layer and the metal contact (Al) from 4.43 to 2.93, 3.02, and 4 eV, respectively, accompanied by enhancements of 35, 27, and 25% in electroluminescence intensity.

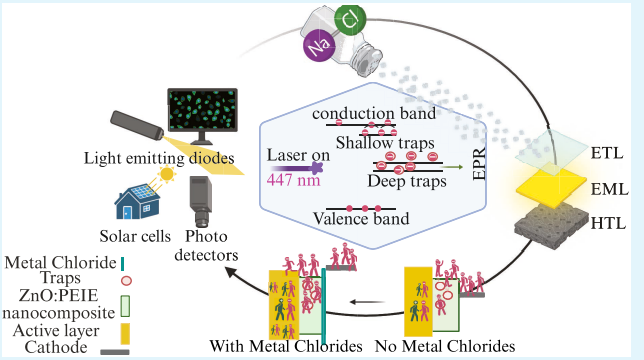

KEYWORDS: *interfacial engineering, metal chlorides, organic electronics, electron paramagnetic resonance spectroscopy, interface dipoles, photoelectron spectroscopy, DFT calculations*

1. INTRODUCTION

Interfaces between different layers have been an area of significant interest and exploration in the field of micro- and nanoelectronic devices.[1] These interfaces play a significant role in a wide range of applications, such as catalysis, sensors, batteries, optoelectronic devices, and more. In-depth understanding of the fundamental principles including the interactions at these interfaces is significant for designing and optimizing novel materials and devices with enhanced performance.[2]

In optoelectronic devices, such as light-emitting diodes (LEDs) and solar cells, the management of charge carriers is of paramount importance.[3] In the context of LEDs, engineered charge injection leads to a flow of charges between the electrodes. Electrons emitted from the cathode recombine with holes injected from the anode in the emissive layer, resulting in light generation.[4] The charge injection can be facilitated by lowering the potential barrier with the subsequent layer. Effective recombination of electrons and holes in the emissive layer results in a higher efficiency and a brighter device.[5] Conversely, for solar cells, the process involves harnessing solar energy. Here, electron−hole pairs created by the absorption of photons from sunlight must be efficiently separated and collected at the electrodes to generate an electric current. Achieving this requires the creation of a potential difference across the interface, a factor that can be finely adjusted through interface engineering. Efficient charge transfer, therefore, is a common denominator in both light-emitting devices and solar cells. It not only leads to higher light output and greater power

Received: September 27, 2024
Revised: October 25, 2024
Accepted: October 29, 2024
Published: November 15, 2024

Downloaded via IMEC VZW on April 8, 2025 at 08:04:38 (UTC).
See https://pubs.acs.org/sharingguidelines for options on how to legitimately share published articles.

© 2024 The Authors. Published by American Chemical Society

https://doi.org/10.1021/acsami.4c16558
ACS Appl. Mater. Interfaces 2024, 16, 65687−65701

output in LEDs but also plays a vital role in effectively converting sunlight into electrical energy in solar cells.[6,7] Various interface engineering strategies exist to enhance the performance of optoelectronic devices including the modification of the material work functions (WFs), charge carrier injection barriers, and reduction of the influence of interface traps. These optimizations can be achieved through physical surface treatments like plasma treatment[7] and ultraviolet ozone (UV) treatment,[8] as well as the incorporation of an ultrathin interfacial layer (approximately 1−10 nm) positioned between electrode and electron (hole) injection layers (E/HIL).[9,10] The interfacial layer functions as an electric dipole layer with a known electric dipole moment, strategically positioned at the interface between the electrode and injection layers. This configuration generates an electric field, effectively adjusting the energy level of the layers by modifying their work function.[11] The electric dipole involves two points with positive and negative charges, which are placed at a distance. An asymmetrical distribution of these charges in an ultrathin layer creates individual single electric dipole moments and finally an electric dipole layer.[12] It is noteworthy to mention that these modifications are not limited to inorganic optoelectronics alone, and they also add positive changes to organic optoelectronic devices. For instance, in organic optoelectronic devices, a self-assembled monolayer of organic molecules like alkyl thiols or phosphonic acids[13] is a common dipole layer that positively changes the materials work function and charge dynamics across the interface.[14] Polyethylenimine ethoxylated (PEIE), an insulator material,[15] modifies the electronic properties of the interface by increasing the charge carrier mobility and reducing the recombination rate of charge carriers close to the electrode regions, thus improving the energy levels at the interfaces.[16] Semiconductors, like molybdenum oxide (MoO_3), as buffer layers have been used to generate an intermediate energy level between two layers of poly(3,4-ethylenedioxythiophene) polystyrenesulfonate (PEDOT:PSS) and CuPc.[17] Alkali metal fluorides like lithium fluoride (LiF)[18,19] and sodium fluoride (NaF) are common materials that can be used as a buffer layer.[19] LiF alters the WF of the electrode, field emission, carrier injection,[20] and contact adhesion, which leads to better stability and performance.[21,22] However, metal fluoride poses health risks and is costly due to processing limitations. Further, they also have very limited charge-trapping and detrapping capabilities on metal oxides. Therefore, an alternative material is needed that can replicate the desirable electronic properties of metal fluorides while being safer, more accessible, compatible with solution processing, and with enhanced charge transfer capabilities. Inorganic alkali metal chlorides (MC) as interfacial layers are one of the best candidates because they exhibit dipole moments similar to LiF, which can be employed in most of the optoelectronic devices such as organic light-emitting diodes (OLEDs) to further improve their performance.[23,24]

In the present work, metal chlorides, including sodium chloride (NaCl), cesium chloride (CsCl), potassium chloride (KCl), and rubidium chloride (RbCl), have been considered to be used in optoelectronic devices like OLEDs. The influence of incorporating metal chlorides in optoelectronic devices on the charge injection capability and device performance has been studied. Based on literature studies, these compounds effectively facilitate the injection of electrons into the organic layers of the OLEDs, leading to improved device performance.[25,26] Another advantage of metal chlorides over alkali metal fluorides is their cost-effectiveness. These compounds can often be produced at a lower cost, making them more economically viable for large-scale production of optoelectronic devices. Furthermore, alkali metal chlorides demonstrate compatibility with various substrates, such as flexible[27,28] and rigid substrates, without significant degradation or loss of performance. For instance, transparent flexible electrodes have been made by the deposition of a NaCl sacrificial crystal on polyethylene terephthalate (PET), which has the advantages of making different sizes of NaCl particles varying from 10 nm to micrometers by adjusting the thickness and substrate type. Additionally, metal chlorides can be deposited by solution processing, such as spin coating and physical deposition techniques, such as vacuum evaporation. For instance, NaCl has been deposited by using atomic layer deposition (ALD) for substrate protection from surface contamination.[28] Finally, the wide range of material options with metal chlorides allows for a wide range of explorations of new combinations. Generally, alkali metal chlorides have better sustainability compared to metal fluorides due to factors like lower cost and recycling ability. Lü and colleagues[29,30] delved into the realm of metal chlorides, inspired by the distinctive traits of alkali metal chlorides. They structured their study around a device architecture involving ITO/*N*,*N*′-di(naphth-2-yl)-*N*,*N*′-diphenyl-benzidine (NPB, 40 nm and BCP, 15 nm)/tris(8-hydroxyquinoline) aluminum (Alq_3) (60 nm)/metal chlorides (1.0 nm and at various distances inside Alq_3)/Al. Within their investigation, they observed a remarkable increase in the light output, specifically in the CsCl devices. Their hypothesis attributed this enhancement to tunneling and the potential barrier reduction.[29,30] Building further on this initial observation, this work explores the mechanism of this enhancement in much more detail using a combination of a wide range of experimental techniques with corroborating simulations and density functional theory (DFT) computations. As such, a detailed understanding is obtained of how metal chlorides as interface layers in OLEDs can significantly boost their performance. We find that these compounds are not just replacements for other materials like LiF, but they excel in enhancing charge transport to the active layers, making devices more efficient. Various complementary techniques were used, such as electron paramagnetic resonance (EPR), impedance spectroscopy, X-ray photoelectron spectroscopy (XPS), ultraviolet photoelectron spectroscopy (UPS), and DFT calculations. Our findings show that adding a metal chloride layer improves several key aspects of the OLED performance, like brighter light, better efficiency, and lower power needs compared to devices without these layers. This is because these layers reduce the influence of interfacial traps that can slow down electrical flow and make it easier for charges to move around. Additionally, the creation of an interface dipole layer lowers the work function of the metal contact, resulting in better electron injection, all confirmed by our different measurements and calculations. The properties of metal/metal chloride/semiconductor interfaces are studied in an OLED stack of ITO/poly(3,4-ethylenedioxythiophene) polystyrenesulfonate (PEDOT:PSS)-hole transport layer, poly(*para*-phenylenevinylene) copolymer (SY)-emissive layer, and ZnO:PEIE nanocomposite (NC) (electron transport layer)/metal chloride (surface modifier)/Al.

In light of our findings, we conducted a comparative analysis among different OLED devices based on CsCl, RbCl, NaCl, and KCl, and a reference device without an interfacial layer,

https://doi.org/10.1021/acsami.4c16558
ACS Appl. Mater. Interfaces 2024, 16, 65687−65701

evaluating their performance in terms of electroluminescence (EL) intensity, external quantum efficiency (EQE), luminous efficacy, illuminance, and current density. Our analysis revealed that devices based on CsCl and RbCl outperformed the devices based on KCl, NaCl, and the reference device in these specific aspects. Therefore, we conclude that CsCl and RbCl are the suitable choice for OLED applications, although KCl and NaCl with a minor difference in respect to the above-mentioned compounds can be true choices for a variety of optoelectronic applications due to abundancy, lower cost, and easy access.

This research sheds light on the importance of interface engineering factors in optimizing optoelectronic device performance and provides valuable insights for future advancements in research and industrial applicability.

2. EXPERIMENTAL SECTION/METHODS

2.1. Materials. BIOTAIN-supplied glass substrates patterned with indium thin oxide (ITO), having a thickness of approximately 135 ± 5 nm, have been utilized for all the OLED samples. These substrates exhibit a sheet resistance of 10^{-15} Ω sq^{-1} as well as a transmittance above 86%. Poly(3,4-ethylenedioxythiophene) polystyrenesulfonate (PEDOT:PSS, grade Al 4083) has been received from Heraeus supplier. Super Yellow (SY) light-emitting PPV copolymer (PDY-132), polyethylenimine 80% ethoxylated solution (PEIE, 37% wt % in H_2O), and zinc oxide nanoparticle (NP) ink containing particles (diameter ≈10 to 15 nm) dissolved in isopropylalcohol (IPA) have been obtained from Sigma-Aldrich. Cesium chloride ≥99.5%, rubidium chloride 99.8+%, and potassium chloride 99% have been provided by VWR Chemicals. 99.99% aluminum pellets have been bought from Kurt J. Lesker, while 99% and 99.99% lithium fluoride were obtained from Alfa Aeser by Thermo Fisher Scientific.

2.2. Device Fabrication. The OLED preparation starts with a thorough cleaning process. The cleaning protocol of the ITO-coated glass substrates involves ultrasonication for 30 min in soap water, 20 min in demineralized water, 10 min in acetone, and finally 10 min in isopropanol alcohol. Afterward, the samples were dried using nitrogen gas and were treated with UV−ozone for 30 min.[31] Spin coating has been used for deposition of all of the active layers. PEDOT:PSS diluted in water has been spin-coated at 2000 rpm for 40 s, resulting in a 40 nm-thick layer. SY dissolved in chlorobenzene (20 mg/4 mL) has been spin-coated at 1000 rpm for 60 s inside a glovebox environment, resulting in 80 nm-thick layers. Finally, ZnO NP ink and PEIE were mixed together (1.5 mL/0.006 mL) and dissolved in 2 mL IPA, which has been deposited at 6000 rpm for 60 s, resulting in 14 nm-thick layers.[31] Subsequently, all the metal chloride/fluoride layers as well as Al (electrode) were deposited by vacuum evaporation at 8.5 × 10^{-7} mbar. The thickness of Al was 80 nm for all samples, and the thickness of metal chlorides was varied between 1 and 10 nm for different studies. The deposition rate was changed between 0.15 and 0.01 A s^{-1} to control the uniform distribution of the metal chloride clusters.

3. RESULTS AND DISCUSSION

3.1. Morphology. First, thin alkali metal chloride films were prepared by vacuum evaporation (see Materials and Methods Section S1). Surface topology measurements were conducted by atomic force microscopy (AFM) using the tapping mode to visualize the surface roughness of the films (2.5 cm × 2.5 cm), see Figure 1. The images show a quasi-uniform distribution of small nanocrystals with an average height of ∼2−6 nm and width of several tens of nm. Figure S1 provides a zoomed-in view of the small nanocrystals, showing some representative examples and their dimensions. Height data was extracted by generating line profiles through the NaCl particles and creating 3D surface plots for visual inspection

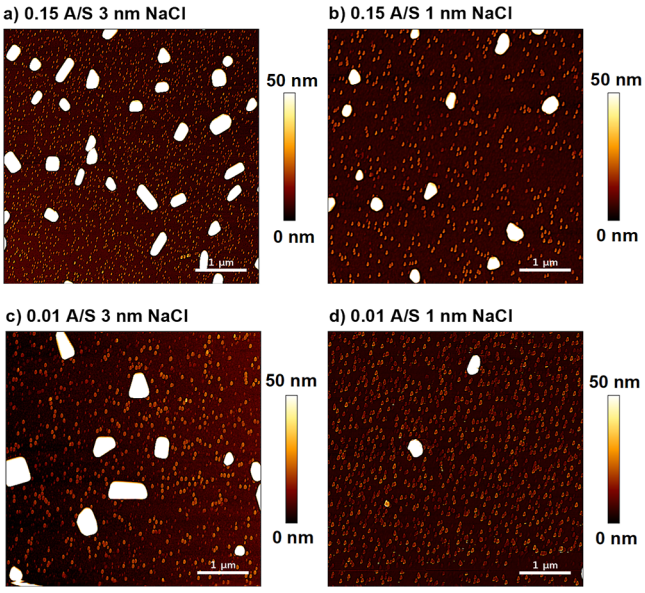

Figure 1. AFM images of NaCl on a glass substrate using different deposition rates of (a) 0.15 A s^{-1} for 3 nm NaCl; (b) 0.15 A s^{-1} for 1 nm NaCl; (c) 0.01 A s^{-1} for 3 nm NaCl; and (d) 0.01 A s^{-1} for 1 nm NaCl.

(see Supporting Information, Figure S1b). Aside from that, larger agglomerates are also found, which seem to be reduced in size and quantity when the deposition rate is reduced from 0.15 to 0.01 Å s^{-1}. Individual particle heights were measured by comparing the maximum particle height to the surrounding substrate level (Figure S1c). Note that in the end, the deposition rate in this range did not significantly influence the final OLED performance. In support of this, Figure S16 demonstrates the similar current density−voltage characteristics of RbCl-based OLEDs fabricated at both low and high deposition rates, underscoring the negligible influence of the deposition rate on electron injection. The metal chloride forms small nanocrystals, even at higher deposition rates. ZnO:PEIE, being a highly efficient electron transport and injection layer, maintains its functionality with minimal impedance from larger metal chloride nanocrystals. This is evident in the consistent current density−voltage characteristics across different deposition conditions. Furthermore, very close and similar electroluminescence performances are observed across both deposition conditions, indicating that the metal chloride nanocrystals do not adversely affect the light emission process of the OLEDs. This supports the conclusion that the electron injection mechanism remains largely unaffected by the variations in the NaCl deposition rate.

Moreover, the robustness of the ZnO:PEIE layer is crucial. The 16 nm ZnO:PEIE layer situated beneath the metal chloride nanocrystals effectively serves as an electron transport layer, ensuring insulation between the organic emissive layer and the cathode. Its thickness and uniformity prevent direct contact between the cathode and the underlying organic layers, significantly reducing the risk of short circuits even in the presence of metal chloride nanocrystals.

In our previous work,[31] we investigated the impact of varying the thickness of the ZnO:PEIE layer on the *J*−*V*−*L* (current density, voltage, and luminance) characteristics of OLEDs. As the thickness of the ZnO:PEIE layer increased from 16 to 28 nm, we observed a reduction in the injected

https://doi.org/10.1021/acsami.4c16558
ACS Appl. Mater. Interfaces 2024, 16, 65687−65701

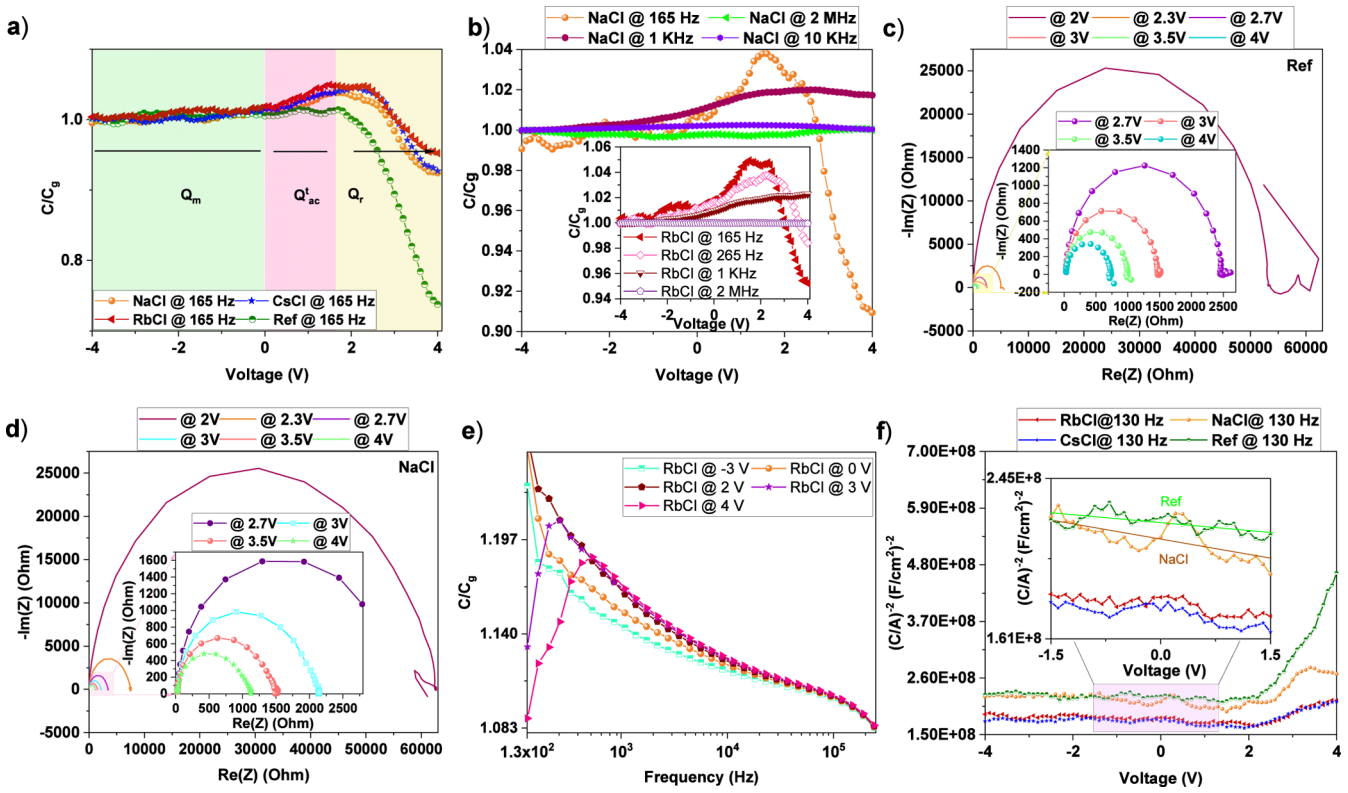

Figure 2. (a) Capacitance−voltage at a frequency of 165 Hz obtained from impedance spectroscopy of OLEDs based on NaCl, RbCl, and CsCl interfacial layers and no metal chloride (reference) showing three regimes including charges in electrodes, charge injection, and recombination of charges; (b) capacitance−voltage at different frequencies from 165 Hz to 2 MHz for OLEDs based on NaCl and RbCl; (c) Nyquist plot of the reference sample at different voltages; (d) Nyquist plot of NaCl-based OLED at different voltages; (e) capacitance−frequency measured at −3, 0, 2, 3, and 4 V; (f) Mott−Schottky profile showing the slope of -8.36×10^{-12} ($(F/(cm)^{-2})/V$) in the range between −1.5 and 1.5 V.

current and luminance. This reduction indicated a disruption in the carrier balance, where the thicker ZnO:PEIE layer impeded efficient electron transport, leading to a lower EQE. We have now referenced this finding in this article, clarifying that the thickness of the ZnO:PEIE layer does indeed affect carrier balance.

3.2. Optical Properties. The transmittance of ZnO:PEIE NC films is illustrated in Figure S2, and the Tauc plot of NaCl on ZnO:PEIE NC layers is depicted in the inset of Figure S2. The results are highly comparable and show that the addition of a thin metal chloride layer does not impact the absorption of light in the OLEDs.

3.3. Charge Transport Properties. We start from impedance spectroscopy, i.e., capacitance−voltage measurements, to provide insights on the influence of different metal chloride interfacial layers on charge-injection and charge-recombination in the OLED device. In such a CV measurement, an alternating electrical signal with a small amplitude V_1 (0.05 V) and a specific frequency f in the range of 20 Hz to 2 MHz ($V_{AC} = V_1 \sin(2\pi ft)$) is superimposed to a constant bias DC voltage (ranging from −4 to 4 V), resulting in a total voltage $V = V_{DC} + V_{AC}$ applied over the device.[32] The response from the sample is measured by the induced AC current. The complex impedance can then be calculated as the ratio of voltage and current from which capacitance C can be obtained. A first increase in capacitance with respect to the geometric capacitance (C_g)[32] in the dark current regime (no light generation of the OLED) arises from the accumulation of charge carriers in the active layers, the latter being composed of the electron transport layer, the emissive layer, and the hole transport layer (HTL). At higher voltages, charge carriers meet in the emissive layer and recombine by emitting a photon, thereby reducing the capacitance.

Impedance spectroscopy has been performed on a complete OLED stack, which is shown in Figure S3. The capacitance−voltage results are presented in Figure 2a, where the measured capacitance is normalized over the geometric capacitance C_g, which can be determined at highly negative voltages and is described by eq 1.[33,34]

$$C_g = (\varepsilon_0 \times A) \times \frac{(\varepsilon_{r\text{-HTL}} \times \varepsilon_{r\text{-EML}} \times \varepsilon_{r\text{-ETL}})}{(\varepsilon_{r\text{-ETL}} \times \varepsilon_{r\text{-EML}} \times d_{HTL}) + (\varepsilon_{r\text{-HTL}} \times \varepsilon_{r\text{-ETL}} \times d_{EML}) + (\varepsilon_{r\text{-EML}} \times \varepsilon_{r\text{-HTL}} \times d_{ETL})} \quad (1)$$

with ε_0 (8.854×10^{-12} F m^{-1}) being the permittivity of vacuum, ε_r the dielectric constant of the active layers, A (0.25 cm^2) the area of the active region of the OLED, and $d_{HTL/ETL/EML}$ the thickness of the hole transport layer (HTL), emissive layer (EML), and electron transport layer (ETL).

Three regimes can be seen in the $C-V$ curve presented in Figure 2a. The first regime (green) at high reverse bias shows the device in insulating (dark) mode, providing the value of the geometric capacitance ($C/C_g = 1$) at the lowest voltages.[35] The average value found for C_g was 1.64 ± 0.1 nF. The relative dielectric constant of the active layers determined by eq 1 for a 40 nm-thick HTL, 200 nm-thick EML, and 16 nm-thick ETL is found to be around 7.8 ± 0.7. Given that the dielectric constants of the EML and HTL in literature are found to be between 2 and 3.5,[36,37] this implies that the dielectric constant

https://doi.org/10.1021/acsami.4c16558
ACS Appl. Mater. Interfaces 2024, 16, 65687−65701

of the ETL should also lie in the range of 2 in our case. To be more accurate, $\varepsilon_{r\text{-HTL}}$, $\varepsilon_{r\text{-EML}}$, and $\varepsilon_{r\text{-ETL}}$ of 1.9 ± 0.1, 2.65 ± 0.05, and 1.55 ± 0.5 could be considered for the OLED stack. Interestingly, the dielectric constant of ZnO nanoparticles in literature is reported to be around 8, while in our case, we find a value around 2, which can most likely be attributed to the reduction in dielectric constant upon ZnO nanoparticle integration within PEIE, similarly as previously observed for other organic materials.[38,39]

The second regime (pink) in Figure 2a shows the expected increase in capacitance with increasing DC voltage, indicating the injection of majority carriers in the active layers and can be represented by Q_{ac}^{t}, which shows the amount of charge trapped in the active layer due to the AC voltage.[35] Specifically in our experiments, the capacitance begins to increase above a threshold voltage of approximately 0 V for the reference sample.[40] Figure 2b demonstrates the capacitance behavior at different frequencies for NaCl- and RbCl-based OLEDs. The threshold voltage observed in Figure 2b appears to be independent of frequency since the initial charge accumulation process is primarily governed by material properties rather than the frequency of the applied AC signal. According to eq 2, which is provided further on, and the explanation provided, the capacitance (C) is influenced by three components:

At the threshold voltage, the system transitions into the second regime, dominated by Q_{ac}^{t}, where charge injection and trapping occur. This threshold is determined by the balance between the applied voltage and the intrinsic properties of the material, such as the energy barriers for charge injection and trapping. Since these material properties are nearly constant, the threshold voltage remains quasi unchanged for different frequencies.[41,42]

The frequency begins to affect the system significantly only in the subsequent regimes. At higher frequencies, charge carriers have less time to migrate and the maximum capacitance shifts to higher voltages, while recombination processes are less likely to occur, see Figure S6. However, the threshold for the initial charge accumulation, i.e., the threshold voltage, does not rely on these dynamic processes and thus remains constant, regardless of the frequency applied. Moreover, at lower frequencies, the AC signal changes slowly, allowing charge carriers ample time to migrate through the active layers of the OLED and become trapped in defect sites or other trapping states. This migration and trapping contribute to an increase in capacitance because more charges accumulate in response to the applied voltage.

As the frequency increases, the AC signal oscillates more rapidly, reducing the time available for charge carriers to respond to a changing electric field. Consequently, fewer charges can migrate through the active layers and get trapped within the time frame of each oscillation cycle. This limited charge movement results in a smaller increase in capacitance as less charge is available to contribute to the overall capacitance of the device.

In addition, at higher frequencies, the charge carriers that do migrate are less likely to reach deeper trapping states because the electric field direction changes before the carriers can fully settle. This incomplete trapping further diminishes the capacitance increase. Additionally, the maximum capacitance shifts to higher voltages at higher frequencies because more energy is required to drive the migration and trapping processes under these conditions.[43]

Therefore, the reduced capacitance increase at higher frequencies is due to the limited time for charge migration and trapping, which are critical processes that contribute to the capacitance. This frequency-dependent behavior is a fundamental aspect of charge dynamics in OLED devices and is essential for understanding the device's performance under different operating conditions. Finally, in the third regime (yellow), a sharp reduction in capacitance is observed, originating from the recombination of charges by emitting a photon, thereby consuming the charge carriers and decreasing the capacitance. The detailed explanation is given in the Supporting Information Section S5.

These three regimes can be identified by eq 2, which describes capacitance as consisting of 3 parts[35,41]

$$C = \frac{dQ}{dV} = \frac{dQ_m + dQ_{ac}^{t} - dQ_r}{dV_{AC}} \quad (2)$$

where Q represents the total change in charge due to the superimposed AC signal (V_{AC}). Q_m defines the typically minor charging of the electrodes, which can result in a small increase of the capacitance in the green regime, while Q_{ac}^{t} dominates in the second region. Finally, Q_r describes the loss of charge due to recombination in the third regime. The recombination rate τ_r as well as the trapping rate τ_{trap} are two important time scales determining the frequency response of the CV signals and, in particular, the competition between charge trapping and charge recombination. Therefore, at higher frequencies, charge carriers do not have sufficient time to migrate in the active layer, resulting in a smaller increase and a shift of the maximum of the curve to larger voltages, as clearly observed in Figure 2a. Recombination can also not take place, resulting in the capacitance not being dependent on voltage anymore.[35]

To study ionic migration (current) in the presence of OLEDs, electrochemical impedance spectroscopy (EIS) is an invaluable tool. In EIS, an alternating current (AC) potential is applied to a device, and the resulting AC current is measured. By analyzing changes in amplitude and phase across a wide frequency range, EIS can distinguish between different processes occurring at various time scales. This makes it particularly useful for investigating both ionic and electronic transport in materials such as hybrid organic−inorganic heterojunctions.

EIS results are typically presented as Nyquist plots. These plots graph the real (Z') and imaginary (Z'') components of impedance in a complex space. The impedance data are conducted at a frequency range of 1 MHz to 1 mHz, a 10 mV perturbation, and several bias voltages, i.e., from 2 to 4 V. Figure 2c,d illustrates the Nyquist plots for reference and NaCl-based OLEDs. Figure S4 provides more detailed information about the Nyquist plots of the OLEDs with various metal chloride interfacial layers at different voltages. Data near the origin corresponds to higher frequencies, while data farther away represents lower frequencies. Analyzing Nyquist plots involves fitting the data to equivalent circuit models to quantitatively assess device properties. The shape of the plot provides insights into the underlying processes: (1) a vertical line suggests a circuit with a capacitor in series with a resistor, with resistance indicated by the x-axis intercept. (2) A semicircle with an origin intercept indicates a parallel combination of a capacitor and resistor. (3) A semicircle shifted along the x-axis implies the presence of a series resistor, with the shift corresponding to the series resistance.

https://doi.org/10.1021/acsami.4c16558
ACS Appl. Mater. Interfaces 2024, 16, 65687−65701

When investigating the influence of metal chloride additives on ionic currents in the presence of OLEDs, impedance plots can reveal both electronic and ionic processes. Typically, Nyquist plots show two distinct features: a semicircle at high frequencies and another semicircle or linear feature at low frequencies. At high frequencies, electronic processes predominate, and these devices can be effectively modeled using a simple electronic RC circuit. At lower frequencies, ionic transport becomes more significant, often represented by the Warburg element, which captures ion diffusion and appears as a 45° diagonal line in the low-frequency region of Nyquist plots.[44,45]

In our study, when analyzing the effect of adding metal chloride on ionic currents, we would expect to see a Warburg element if ionic diffusion is significant (refer to Figure S4e,f). However, our measurements reveal only a single semicircle and lack the expected 45° tail, suggesting that ionic contributions might be minimal or not adequately captured in the frequency range tested. Additionally, no significant difference is observed between the reference and salt-treated samples in the low-frequency region. This absence of the Warburg element and the lack of notable differences imply that ionic diffusion is not prominent or that the metal chloride addition has not significantly influenced ionic transport in the OLED device.

For the OLEDs with and without metal chloride interfacial layers, the following results are observed and listed in Table S1.

Capacitance values with metal chloride interfacial layers, which are listed in Table S1, are comparable to or slightly higher than those with the reference OLED. The variations in C_{ct} suggest that metal chlorides affect the dielectric properties and charge storage characteristics of the OLED, though the impact on capacitance is relatively modest.

In summary, NaCl, RbCl, and CsCl enhance the performance of an OLED by reducing series resistance and influencing charge transfer characteristics. The capacitance changes are relatively minor, reflecting the impact of the interfacial layers on the OLED's electrical properties. Additionally, R_{series} in our OLED devices does not show significant variation with different applied voltages or over time (nearly 20 h of operation), suggesting that series resistance is stable and not heavily influenced by factors like ion accumulation, which complements the earlier discussion of not observing the Warburg element. If R_{series} increases with applied voltage, it may indicate ion accumulation at the device's contacts affecting resistance. However, the stability in R_{series} in our devices implies that ion accumulation is not a significant issue, and thus, ionic current may not significantly impact the OLEDs.[46]

Figure 2e illustrates the capacitance as a function of frequency for different DC voltages. At reverse bias conditions, e.g., −3 V, no charges are injected, and the capacitance remains constant across the frequency regime, yielding the geometric capacitance of the device. The device behavior is like a dielectric layer at high reverse bias as a nearly independent relationship from capacitance can be observed.[35,47] At higher DC voltages, this peak shifts to higher frequencies, thus resulting in first an increase and then a decrease in capacitance related to the carrier trapping and radiative recombination, respectively. The exact frequency dependence and position of the peak can yield information on the relative time scales between trapping and charge built-up in the devices and recombination of charges in the emissive layer, two processes that are in competition when the device is turned on. Equation 3 details these two processes and provides a way to extract information on the trapping and recombination rates. The derivation of eq 3 is explained in the Supporting Information, Section S5

$$C(\omega) = C_g + \frac{\chi_1 C_g}{1 + \omega^2 \tau_{trap}^2} - \frac{\chi_2 C_g}{1 + \omega^2 \tau_r^2} \tag{3}$$

with $\omega = 2\pi f$. The first term represents the geometric capacitance C_g; the second term represents the time it takes for carriers injected under forward bias ($V_{DC} > 2$ V) to become trapped, leading to an increase in capacitance in the lower frequency region of the $C-V$ curve and thus depending on (τ_{trap}); and the third term represents the decrease of capacitance at slightly higher frequencies, related to the recombination rate (τ_r), which dominates at higher voltages ($V_{DC} > 3$ V). χ_1 and χ_2 are dimensionless constants. A minimalization process that adjusts the parameters (χ_1, χ_2, τ_{trap}, and τ_r) was applied to adequately fit the experimental data points. When fitting the experimental data to eq 3, it should be noted that the different parameters are correlated due to the intrinsic nature of the equation, where the second and third components have opposite signs. Therefore, the trapping and recombination times can be estimated only within a certain error margin. Figure S5 shows the fits for voltages from 2 to 4 V for all the OLEDs. From these fits, it can be concluded that the recombination time is between 10^{-3} and 10^{-2} s and that the trapping time is between 10^{-4} and 10^{-3} s. As shown in Figure S5e, the reduction in trapping times with an increase in voltage in the range of the corresponding OLEDs can be understood through the framework of the Poole−Frenkel effect. At lower voltages, where the electric field strength is weaker, the mobility of charge carriers is limited, and they may become trapped at defects within the OLED material. As the applied voltage, or electric field strength, rises, the energy imparted to charge carriers also increases and enables trapped carriers to overcome potential energy barriers more readily.[48] Consequently, the trapping time decreases as the voltage increases, reflecting the enhanced mobility of carriers under higher electric field conditions.

In fact, the much slower recombination rate with respect to the trapping time implies that the recombination of charges is limited by the injection of electrons in the emissive layer.[35,49]

To further investigate the role of added interfacial layers on charge trapping within an OLED device, a Mott−Schottky plot from the $C-V$ measurements has been plotted in Figure 2f, i.e., plotting $(C/A)^{-2}$ as a function of voltage for a frequency of 130 Hz. In order to calculate the density of filled or electrically active traps (N_t) in the layer, we can employ eq 4, whose derivation is demonstrated in Supporting Information

$$\left(\frac{A}{C}\right)^2 = \frac{2}{q\varepsilon_0\varepsilon_r N_t}\Delta V \tag{4}$$

with q being the elementary charge. The slope of the Mott−Schottky plot in the range where we have charge built-up with increasing voltage (region two in Figure 2a) then corresponds to the inverse of the density of filled traps and amounts to $(7.40 \pm 1.3) \times 10^6$ and $(3.00 \pm 0.7) \times 10^6$ V/F for devices with a 3 nm NaCl layer and the reference without NaCl, respectively. Table S2 provides the slope and trap density values for all of the metal chloride-based OLEDs. By extracting the effective ε_r of the full active layer (ETL, HTL, EML, and

https://doi.org/10.1021/acsami.4c16558
ACS Appl. Mater. Interfaces 2024, 16, 65687−65701

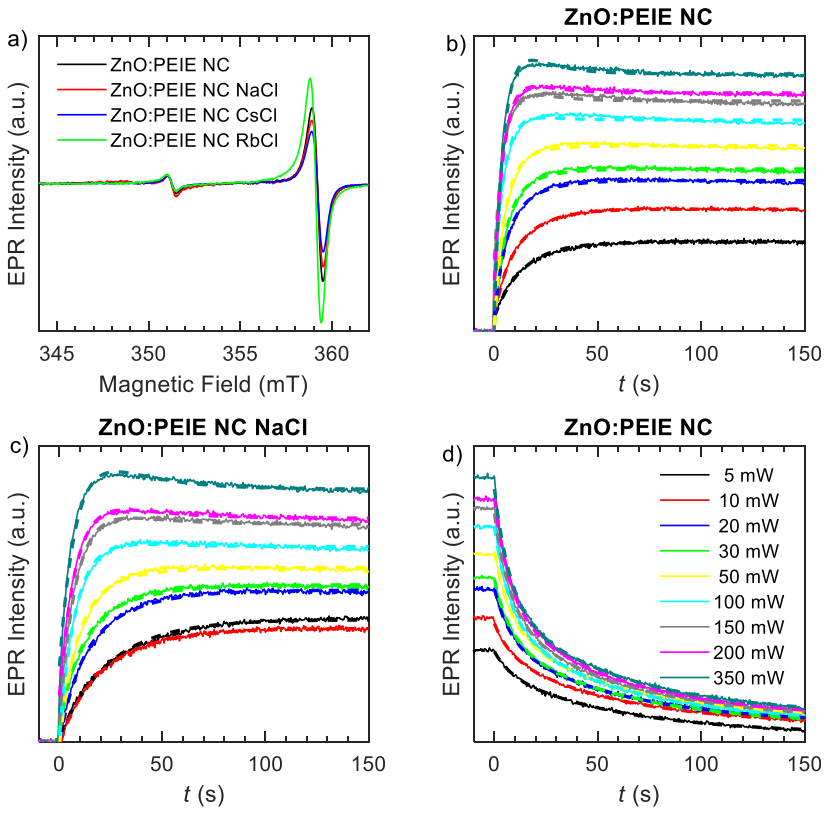

Figure 3. (a) Steady-state EPR signals for different systems including ZnO:PEIE and metal chlorides under light illumination (447 nm, P = 350 mW) and normalized on the intensity of the 351 mT EPR peak. (b,c) Trapping kinetics during illumination at different laser powers for ZnO:PEIE NC and ZnO:PEIE NC NaCl samples (other samples can be found in Figure S10 in the Supporting Information). Experimental data are plotted in solid lines; fitted data are superimposed in dashed lines, while the colors indicate the used laser powers, as presented in the legend of panel (d). (d) Recombination/detrapping kinetics for ZnO:PEIE NC with NaCl using the same line coding as in panels (b,c). Additional data can be found in Figure S11 for the other samples.

NaCl) from the geometric capacitance $C_g = \frac{A\varepsilon_0\varepsilon_r}{d}$, we obtain ε_r = 1.2.[32,34] The number of trapped charges in the experiment for this specific frequency can then be determined and amounts to $(1.60 \pm 0.3) \times 10^{23}$ traps/m^{-3} for the OLED with NaCl and to $(4.00 \pm 0.6) \times 10^{23}$ traps/m^3 for the reference OLED. This seems to indicate that addition of metal chlorides prevents the existing traps in active layers from being filled, resulting in a better transport of charges across that layer.

To investigate this in more detail, we performed time-resolved electron paramagnetic resonance (TR-EPR) measurements, focusing in particular on the ETL composed of metal chloride/ZnO:PEIE NC. First, we present steady-state continuous-wave EPR of mixtures of different metal chlorides with ZnO:PEIE NC. The mixtures were prepared by drop-casting a mixed solution of 0.006 mL of PEIE, 1.5 mL of ZnO, and 2 mL of IPA on a glass substrate and 0.4 mg of salt in 4 mL of methanol, after which the glass substrate was cut into small pieces and assembled inside an EPR quartz tube. As such, an EPR powder spectrum is obtained. ZnO NPs are known to contain a lot of intrinsic defects where charges can be trapped,[50,51] which can be observed at room temperature in EPR. ZnO EPR signals typically consist of two main EPR lines,[31,52] one at g = 2.003 (B = 351 mT) and one at g = 1.96 (B = 359 mT). Since the peak observed at 351 mT is quasi-insensitive to light illumination (similar intensity when measuring in the dark or under strong (P = 350 mW) 447 nm laser excitation, see Figure S9), its peak intensity was chosen to normalize the different samples with respect to each other as the quantity of ZnO in each of the EPR sample tubes could not be taken exactly the same. Moreover, a microwave power of 20 mW was chosen for all EPR measurements; given the higher microwave powers, the 351 mT signal was fully saturated (see Figure S8). Samples were illuminated at a power of 350 mW, for which each of the samples showed a saturated EPR intensity (Figure S9).

Figure 3a presents the EPR data under light illumination. Previously, we found that the addition of PEIE to ZnO nanoparticles significantly increased the 359 mT peak, even though PEIE itself has no EPR signal.[31] Here, we find that the addition of salt also alters the relative EPR intensity of the peak at 359 mT. These changes in the response of the EPR signal upon light illumination (see Figure S9) could point at changes in the competing time scales of charge trapping (after creation of charges by the light illumination) and charge detrapping/recombination, requiring a more in-depth investigation through time-resolved EPR. In this case, the EPR signal is monitored at a fixed magnetic field (peak of the EPR signal around 359 mT) as a function of time while putting the light illumination on and off at different laser powers. While the time scale of charge creation and trapping can be observed when monitoring the rise of the EPR signal after the light has been put on, the charge recombination time scales can be obtained by monitoring the decrease of the EPR signal after the light has been put off. We moreover perform these experiments as a function of laser power to provide evidence

https://doi.org/10.1021/acsami.4c16558
ACS Appl. Mater. Interfaces 2024, 16, 65687−65701

that the specific laser power has no effect on these time scales (see further).

Figures 3b,c and S10 present the trapping kinetics during illumination after starting the illumination (with different laser powers) at time $t = 0$, while Figures 3d and S11 hold the information on the recombination kinetics after stopping the illumination at time $t = 0$. To understand the kinetics observed, we base ourselves on ref 53, where similar observations have been made for TiO_2 nanoparticles under light illumination.

Note that the bandgap of ZnO:PEIE is approximately 3.37 eV, and thus, the laser energy of 2.77 eV cannot directly excite across the bandgap, indicating that the optical excitation excites the electron to defect levels in the band gap. Previous fluorescence studies of ZnO:PEIE indeed indicated the emission from different defect states with varying energy in this particular energy range,[31] indicative of a wide range of trap energies within the bandgap of ZnO; the exact nature of these traps is not yet known.

The model in ref 53 bases itself on the following trapping kinetics. After optical excitation, an electron and hole are formed, and a fraction of these will directly recombine again, leaving no effect on the EPR signal. The electrons can become trapped in either shallow or deep traps at or near the surface of the nanoparticle. The electrons trapped in the deep defects remain trapped for a sufficiently long time to be measured by EPR. The electrons caught in the shallow traps will move from trap-to-trap through hopping until a carrier of opposite sign is encountered, resulting in recombination, or until a deep trap is encountered, resulting in an increase of the EPR signal, yet at a longer time scale. This moving carrier in the shallow traps is EPR-silent. In this case, the trapping kinetics can be described by a biexponential rise of the EPR signal, including a fast rise component (k_1) originating from the direct carrier trapping in the deep traps and a slower component (k_2) related to the chance of finding an unoccupied deep trap for the moving electrons, thus resulting in a slower increase at longer times and eventually a saturation at the highest laser powers (all traps filled). Such a model results in eq 5[53]

$$y(t) = y_0 + C_1(1 - e^{-k_1 t}) + C_2(1 - e^{-k_2 t}) \quad (5)$$

with y_0 being the offset and C_1 and C_2 parameters that depend on the laser power and starting configuration, while k_1 and k_2 are supposed to be laser power-independent and can thus be used as global fitting parameters for all power-dependent data. Thus, k_1 and k_2 are fitted simultaneously to all data of the different laser powers and optimized numerically by a nonlinear least-squares algorithm, while y_0, C_1, and C_2 are each time determined analytically for each of the laser powers separately. The so-obtained curves fit the data quite well, as exemplified by superimposing the fit curves on the experimental data in Figure 3b,c for ZnO:PEIE with NaCl (while Figure S10 in Supporting Information shows the data for all samples).

A second set of experiments, presented in Figures 3d and S11, show the recombination kinetics, resulting in a decrease in the EPR signal. When the illumination is stopped, electron−hole recombination or detrapping of the electron can occur, all resulting in a reduction of the EPR signal at different time scales. Given that a model with two different time scales can fit the data very well, we use eq 6 to fit our data[53]

$$y(t) = y_0 + C_3 e^{-k_3 t} + C_4 e^{-k_4 t} \quad (6)$$

In this case, y_0 represents the fraction of unrecombined trapped electrons at a long time. Thus, also in this case, y_0, C_3, and C_4 are fitting parameters for each laser power as each laser power will result in a different configuration of trapped electrons and holes, while k_3 and k_4 should be the same for all the measured laser powers.

Table 1 provides the fitted rate constants for the different salt additions. Interestingly, the addition of metal salt

Table 1. Fitted Parameters for the Different Rate Constants, Expressed in Units of 10^{-3} s^{-1}

	ZnO:PEIE NC	ZnO:PEIE NC NaCl	ZnO:PEIE NC CsCl	ZnO:PEIE NC RbCl
	Trapping Kinetics in ZnO			
k_1	210.2 ± 2.9	123.5 ± 1.3	197.8 ± 2.4	142.2 ± 1.6
k_2	71.4 ± 2.0	41.40 ± 0.77	33.7 ± 1.0	33.1 ± 12.0
	Recombination/Detrapping Kinetics in ZnO			
k_3	133.1 ± 1.7	103.9 ± 1.9	161.9 ± 1.4	116.6 ± 1.2
k_4	17.75 ± 0.20	14.36 ± 0.25	20.45 ± 0.17	18.51 ± 0.11

significantly reduces k_1 and k_2, meaning that the trapping of charges is significantly slowed when adding the metal salts. Such reduction in trapping rate reflects itself in a smaller chance of trapping the electron in the ETL in a working device and thus a more efficient charge transport into the emissive layer. This agrees with the Mott−Schottky analysis in the previous section, where it was found that the density of filled traps was reduced by a factor of 2 for NaCl with respect to the reference sample without metal salt. Figure S12 in the Supporting Information shows for each of the samples and laser powers the ratio of the fast trapping component with respect to the slower trapping component (C_1/C_2). For low excitation powers, the fast trapping dominates, which is logical due to the availability of a large number of empty deep traps; however, at higher excitation powers, the deep traps become fully occupied, making the slow hopping-dependent trapping more important.

Finally, the detrapping/recombination kinetics is also slightly reduced upon salt addition.

3.4. Energy Dynamics. As mentioned in the Introduction section, the addition of an interfacial dipole layer between the electrode and ETL lowers the potential barrier. To investigate this in more detail, the modification of the work function caused by CsCl, RbCl, NaCl, and KCl has been investigated by UPS/XPS measurements and verified by complementary DFT calculations.

To gain insight into the underlying mechanisms of the NaCl behavior as an interface dipolar layer, an accurate prediction of band level alignment at the junction of metal/metal chloride can be obtained by DFT calculation.[54]

To study the influence of NaCl on the energy levels of Al (Figure S13c), DFT calculations have been done on the Al(100) surface with a 3 × 3 supercell. The bond distances between Na and Cl and Cl (Na)−Al were taken as 2.87 and 2.2 Å, respectively, as obtained from ref 55 (other details can be found in Table S3 in the Supporting Information). From an experimental point of view, the work function of a material is a measure of the energy required to remove an electron from the surface of the material. It plays an important role in determining the efficiency of charge injection and extraction in OLEDs since the work function of the electrode affects the alignment of the energy levels of the different layers in the

https://doi.org/10.1021/acsami.4c16558
ACS Appl. Mater. Interfaces 2024, 16, 65687−65701

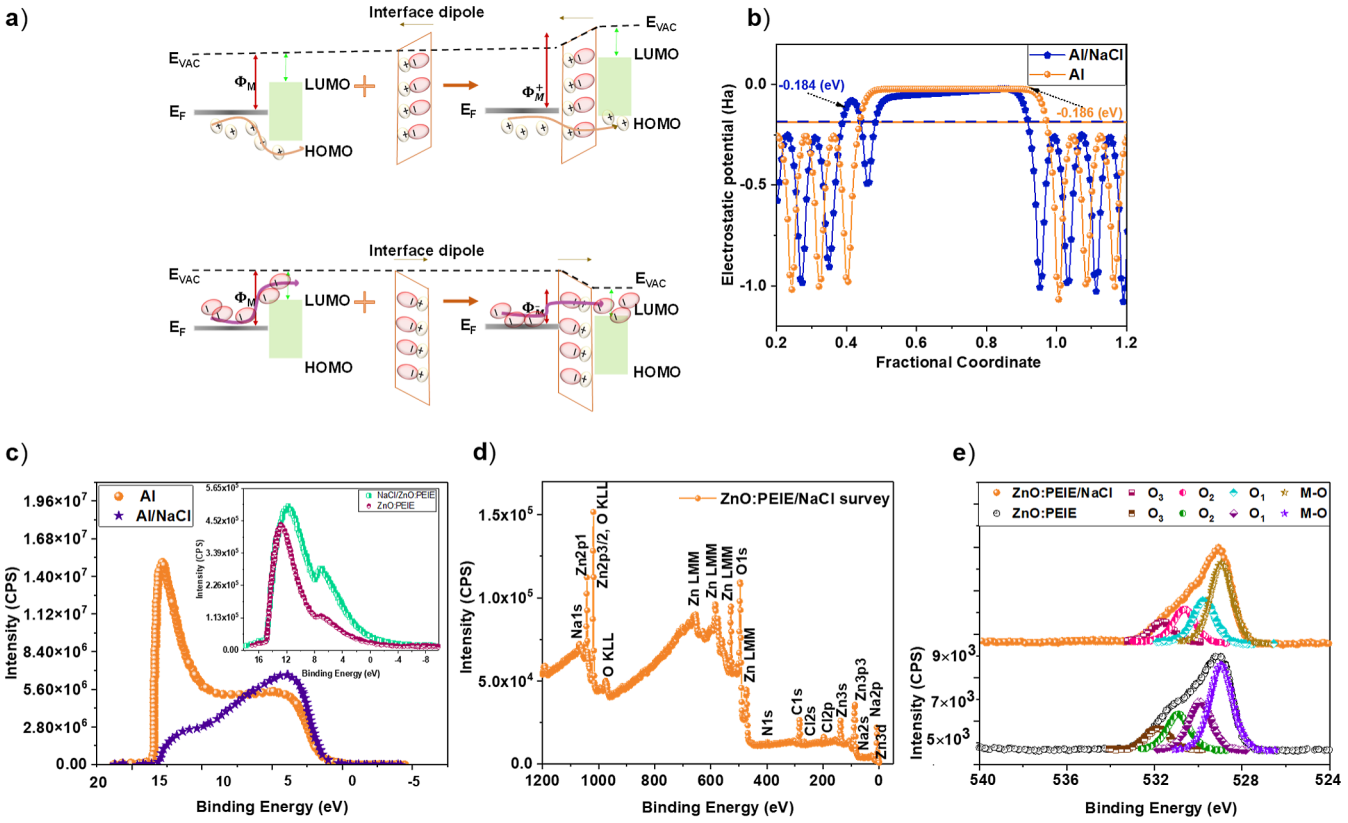

Figure 4. (a) Illustration of interface dipole influence on the energy levels; the upper yellow line shows the lowest unoccupied molecular orbital (LUMO) and the below line demonstrates the highest occupied molecular orbital (HOMO); EI indicates the electron injection barrier and HI shows the hole injection barrier; plus and minus signs refer to the positive and negative sides of the dipole, respectively; (b) electrostatic potential profile between the Al(100) plane and NaCl in vacuum. A band bending originating from the interface dipole behavior of NaCl is shown; (c) UPS spectra of Al and Al/NaCl interface. $E_{\text{cutoff (Al)}} = 12.61$ eV < $E_{\text{cutoff (Al NaCl)}}$ 12.93 eV. The inset picture shows the UPS spectra of ZnO:PEIE NC and ZnO:PEIE NC/NaCl interfaces; (d) XPS survey for chemical quantification of the ZnO:PEIE NC/NaCl system. (e) O 1s high-resolution spectra for ZnO:PEIE NC and ZnO:PEIE NC/NaCl with fitted curves (additional data can be found in Figure S15).

device. The interface dipole plays a crucial role in modulating the local electric field at the surface of a material, thereby influencing its work function.

When the interface dipole has its negative end facing the metal electrode, it generates an electric field that points from the metal toward the interface. This situation effectively creates an additional electric field component that opposes the movement of electrons into the metal. As a result, the work function of the metal is reduced. This reduction in the work function means that electrons in the metal need to overcome a smaller energy barrier to move into the adjacent layer, facilitating easier electron injection. This can significantly enhance the efficiency of charge injection, which is particularly beneficial in electronic and optoelectronic devices, where effective charge transfer is crucial.

Conversely, when the positive end of the dipole faces the metal electrode, it creates an electric field that points from the interface toward the metal. In this case, the positive end of the dipole repels positive charges (holes) and attracts negative charges (electron) into the metal. This orientation increases the work function of the metal by raising the potential barrier that electrons need to overcome to enter the metal. Consequently, the higher work function creates a greater barrier for electron injection, which can hinder the efficiency of charge transfer and negatively impact the performance of the device, Figure 4a. Thus, in the case of the metal chloride interfacial layer, its presence on the surface of the electrode (Al) could lead to the formation of an interface dipole that affects the work function of the electrode.[11]

According to the DFT calculations, the electrostatic potential, which is presented in Figure 4b for Al and NaCl/Al and which explains the distribution of charges perpendicular to the plane as calculated by Kohn−Sham via CASTEP,[56] shows that indeed NaCl molecules significantly change the work function of the Al layer. When using a perfect perpendicular orientation where Cl is closest to Al and Na is pointing upward (as in Figure S13c), the work function of Al is modified from 4.43 to 4 eV for NaCl, 3.02 eV for CsCl, 2.93 eV for RbCl, and 3.15 eV for KCl, respectively (see Table S3).

The DFT calculations also show that the adsorption energy, calculated as the total energy of the hybrid minus the energy of the individual components, is indeed negative and amounts to $E_{\text{adsorption}} = -1.35$ eV, evidencing that this specific configuration is energetically favorable; refer to Table S3 for more details. The $E_{\text{adsorption}}$ value, when calculated for the Na (down) Cl up structure, indicates a negative value of −0.85. This signifies less favorable behavior compared to the Cl (down) and Na (up) structure. In this arrangement, the face of sodium is oriented toward the aluminum plane. This observation supports the dipole layer working principle outlined in Figure 4a.

By performing UPS and XPS measurements, the work functions of the Al, NaCl/Al, ZnO:PEIE NC, and ZnO:PEIE NC/NaCl samples have been measured experimentally. Figure

https://doi.org/10.1021/acsami.4c16558
ACS Appl. Mater. Interfaces 2024, 16, 65687−65701

4c presents the UPS experiments. By determining and comparing the kinetic energies of the electrons emitted from the valence band of the Al electrodes without and with NaCl present, a reduction of the WF of the Al with the NaCl electrode compared to the bare Al electrode is observed. The aforementioned reduction amounts to 0.324 eV (see Table 2),

Table 2. Detailed Information from UPS and XPS Measurements (E_F = Fermi Level, E_{Cutoff} = Electron Cutoff Energy, and E_{VBM} = Valence Band Maximum)

material	E_{Cutoff} (eV)	E_{VBM} (eV)	E_F (eV)
ZnO:PEIE NC	14.50	9.36	1.65
ZnO:PEIE NC/NaCl	14.50	9.31	1.26

which is in remarkable good agreement with the DFT calculations, even though the DFT calculations assume a perfectly stacked arrangement of NaCl molecules, which experimentally is of course not feasible. The reduction of the WF when NaCl is present at the surface of the Al electrode can thus be explained by the formation of an interface dipole layer on the Al electrode surface.

Figure 4d depicts the XPS results obtained for ZnO:PEIE NC/NaCl (detailed images in Figure S14 and data in Tables S4 and S5). In Figure S14, we present the corresponding ZnO:PEIE NC survey. The N 1s spectrum of PEIE from neutral anime nitrogen is located at 400 eV, as also observed by others.[34] The N 1s peak at 400 eV is ascribed to the N−CH_2−CH_2OH tertiary amine caused by the attached electron-rich alcohol hydroxyl end groups. Deconvolution of O 1s and C 1s is presented in Figures 4e and S15, respectively. Regarding the O 1s peak, the 528.7 eV peak originates from oxygen atoms within a fully oxidized environment (M−O). The peak observed at a binding energy of 529.8 eV (O1) is assigned to the presence of the O^{2-} ions within a stoichiometric wurtzite ZnO lattice. Oxygen vacancies (O_2) have been attributed to the peak at 531 eV. The peak at 532 eV (O_3) originates from the presence of loosely bound oxygen on the surface, attributed to H_2O and OH groups integrated into the materials such as hydroxyl groups (M−OH).[57] The observed subtle shifts in the position and intensity of the O_2 peak after introduction of NaCl to the ZnO:PEIE NC system can complement the EPR measurements as the changes in energies of these oxygen-related defects may cause the changes in the trapping and detrapping times observed in EPR. Figure 4d also shows Zn $2p_{1/2}$ as well as Zn $2p_{3/2}$ around a binding energy of 1044 and 1022 eV, respectively.[58] Na and Cl were also detected in the ZnO:PEIE NC/NaCl sample, confirming the correct incorporation of the chloride atoms at the ZnO:PEIE NC surface. The peak fitting of Zn LMM and C

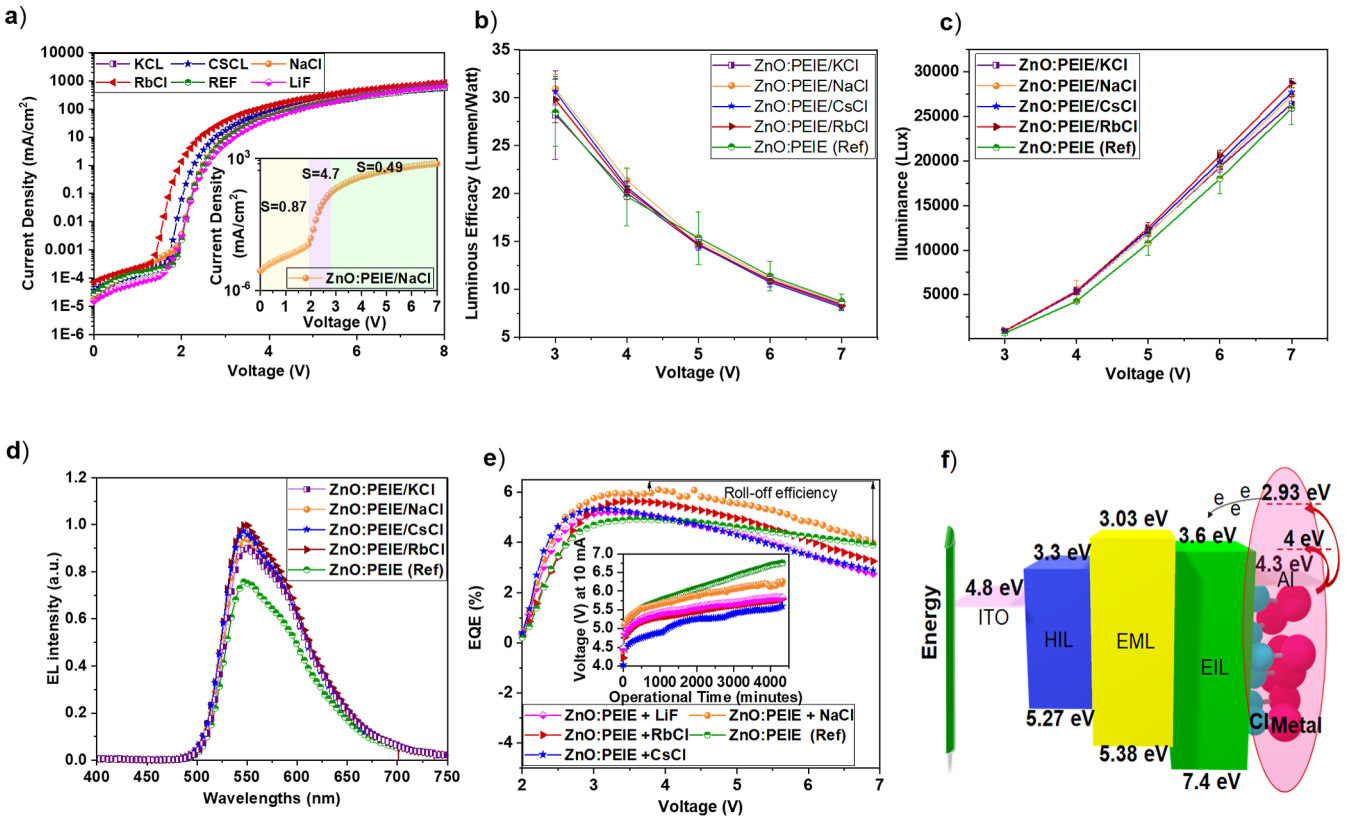

Figure 5. (a) Current density versus voltage of OLEDs based on CsCl, RbCl, NaCl, and KCl metal chloride and LiF interfacial layers. Devices based on RbCl and CsCl demonstrate higher current densities with respect to their other counterparts; (b) luminous efficacy versus voltage for OLED devices based on interfacial layers as compared to a reference sample without the metal chloride layer. Note that error bars represent statistical errors for a set of 5 devices; (c) illuminance versus voltage for OLED devices based on interfacial layers as compared to a reference sample without the metal chloride layer. Note that error bars represent statistical errors for a set of 5 devices; (d) electroluminescence versus wavelength for OLED devices at 7 V, for which a significant improvement can be observed in metal chloride-based OLEDs; (e) external quantum efficiency as a function of voltage for OLED devices. NaCl-based OLED demonstrates the highest EQE at 3 V. The inset of (e) demonstrates the lifetime measurements on fabricated OLEDs; (f) energy level diagram of the OLED devices with metal chloride interface layer.

https://doi.org/10.1021/acsami.4c16558
ACS Appl. Mater. Interfaces 2024, 16, 65687−65701

1s is reported in Figure S15. There are no significant changes observed for the systems with or without metal salt addition, indicating no effect on the Zn vacancies in ZnO upon incorporation of the metal salts.

Prior studies have indicated that the predominant contributors to surface defect sites in ZnO are oxygen vacancies[59] and that these also give rise to the EPR spectra observed in Figure 3.[60] Both Na^+ and Cl^- have been observed to interact with these vacancies on the ZnO surface, forming distinct chemical bonds.[61,62] The UPS analysis of ZnO and ZnO−NaCl samples reveals an upward shift of the Fermi level (E_F), moving it away from the valence band maximum (VBM), which could be ascribed by this interaction between Na^+ and Cl^- ions and ZnO. This adjustment of E_F has the potential to enhance the efficiency of the electron transport process by mitigating energy losses.

In summary, this detailed investigation has revealed that the addition of metal chloride interfacial layers, specifically CsCl, RbCl, NaCl, and KCl, induces changes in the work function of the Al electrode primarily through the formation of an interface dipole. This alteration of the work function has been validated through both DFT calculations and experimental measurements using UPS and XPS. Moreover, TREPR measurements, focusing exactly on these oxygen-related defects, have provided insights into the trapping and detrapping dynamics of electrons at the interface of ZnO:PEIE NC and metal chlorides, thereby enhancing transport of charge through this layer. This observation, coupled with Mott−Schottky plots demonstrating a lower number of filled traps in NaCl-based OLED devices, suggests improved charge transfer through a faster electron current from the electrode to the emissive layer. These findings, particularly in the context of ZnO:PEIE NC systems, highlight the significance of interface engineering in influencing the charge carrier behavior. Moving forward, these insights will be crucial in understanding the potential impact on optoelectronic device performance. The interface dipole-induced changes in the work function and the observed dynamics of charge carriers contribute to understanding how these changes can enhance the overall performance of the OLED devices such as illuminance, luminous efficacy, and external quantum efficiency.

3.5. Device Properties. The advantages of metal chloride interfacial layers in optoelectronic devices over conventional devices (without addition of these layers) have been investigated by comparison of electrical and optical properties of OLED devices. The general device configuration of the OLEDs is ITO/PEDOT:PSS (40 nm)/Super Yellow (80 nm)/ZnO:PEIE NC (16 nm)/metal chlorides (3 nm)/Al (80 nm). Detailed information about all fabricated devices and optimized thicknesses has been summarized in Table S6. A statistical set of 5 samples was measured to obtain an error bar on the device properties. The semilogarithmic graph of the current density−voltage ($J-V$) is presented in Figure 5a. All fabricated OLEDs follow the ohmic behavior at lower voltages, trap-filled limited current at medium voltages, and space charge-limited current behavior at higher voltages (Mott−Gurney), indicated by the different colored regions in Figure 5a. The slope of the $J-V$ curve in the ohmic region represents the series resistance of the device, and it can be calculated as the inverse of the slope of the curve.[31] A slight reduction in the turn-on voltage of RbCl-, CsCl-, and NaCl-based OLEDs with respect to the reference sample can be observed, which is in agreement with the results discussed in the previous sections and caused by lowering the barrier height between the electrode and electron injection layer (EIL). The current density of LiF-based OLEDs has been provided as a common reference, highlighting the enhancement achieved by using metal chlorides instead of LiF. This improvement reinforces the benefits and potential of the present work. The illuminance and luminous efficacy of the OLEDs are presented in Figure 5b,c, with a remarkable increment in metal chloride-based OLEDs compared to reference OLED without an interfacial layer. The highest illuminance at 7 V is observed for RbCl- and CsCl-based devices, being around 28,736 and 27,720 Lux, respectively, followed by NaCl- and KCl-based devices (27,397 and 26,435 Lux, respectively) and significantly stronger than the reference devices without an interfacial layer (25,930 Lux). Table S6 demonstrates an almost 11% increment in illuminance and a 35% increment in irradiance by the addition of RbCl to the reference device without an interfacial layer. Irradiance is defined as the radiant flux received by a detector area, measured in W/m^2, and illuminance is defined as the luminous flux received per unit area of the detector, measured in lux (lm/m^2). The relation between irradiance and illuminance is shown in Supporting Information. Figure 5d presents the electroluminescence spectrum of the devices, while Figure 5e presents the EQE of the devices as a function of applied voltage. The main mechanism behind the enhanced electroluminescent performance of the OLEDs by the insertion of metal chloride layers can be explained by the deactivation of charge traps, therefore aiding in the availability of electrons and holes to recombine in the active layer. The origin of this deactivation can be from multiple factors. First of all, the metal chloride can modify the interface between ZnO and the emissive layer, e.g., by reducing the interfacial resistance or enhancing the charge transfer between these layers, thereby leading to an improved charge injection, which in turn enhances the overall electroluminescent efficiency. As evidenced by EPR spectroscopy and CV experiments, the reported salts change the dynamics of the charge trapping and detrapping mechanisms and passivate the electrically active trap states at the ZnO/emissive layer interface. Traps can be sources of nonradiative recombination, which reduces electroluminescence. By passivation of these defects, metal chloride can help in improving the radiative recombination efficiency. Finally, as evidenced by XPS/UPS and DFT calculations, the metal salts help in optimizing the energy barrier for electron injection from Al into ZnO. Metal chlorides, being an insulating material, could introduce surface dipoles at the interface. These dipoles affect the local electronic environment and reduce the injection barrier for electrons from the Al electrode into the ZnO layer. This results in better alignment and a more efficient electron injection.

The lower electroluminescence intensity of NaCl-based devices compared with other metal chlorides can be attributed to the combined effect of active trap density and interface energy. While NaCl has the lowest active trap density, indicating fewer trapping centers that could quench light emission, the performance could be limited by the work function difference between the NaCl layer and the cathode. NaCl, as indicated by the DFT calculations in Table S3, has a relatively moderate work function, and the adsorption energy at the Al(100)/NaCl interface is lower than that of CsCl or RbCl, possibly resulting in a less efficient charge injection.

In contrast, while RbCl has a higher active trap density, the work function at the Al(100)/RbCl interface (2.93 eV) and its

https://doi.org/10.1021/acsami.4c16558
ACS Appl. Mater. Interfaces 2024, 16, 65687−65701

favorable adsorption energy (−0.57 eV) may improve electron injection, thus partially offsetting the effect of more active traps and maintaining a better EL spectrum intensity. CsCl presents an intermediate case with moderate active trap density and reasonable interface properties, leading to balanced EL performance. Therefore, the differences in EL intensity for these metal chloride-based devices are a function of both the active trap density in the ETL and the binding energy at the EIL/cathode interface. The EQE of the devices improved after the addition of metal chloride layers, showing an increase of approximately 20% in the NaCl device compared to the reference devices. Among the tested materials, the devices modified with NaCl exhibited the highest peak efficiency, reaching 6.11% at 3.9 V (Table S7). At 7 V, the efficiency decreased to 3.98%, leading to a roll-off efficiency (decrease in the efficiency of the OLED device as the current density or brightness increases) of 65.13%. This relatively moderate drop indicates that NaCl maintains better performance stability at higher voltages compared to those of other surface modifiers. In contrast, devices modified with RbCl, CsCl, and LiF showed significantly higher roll-off efficiencies, with efficiencies dropping by around 44−47%. Specifically, RbCl-modified devices saw their efficiency drop from 5.65% at 3.5 V to 3.25% at 7 V, resulting in a roll-off efficiency of 57.52%. CsCl showed similar behavior, with its efficiency declining from 5.34% at 3.1 V to 2.88% at 7 V, corresponding to a roll-off efficiency of 55.06%. LiF-modified devices also experienced a substantial drop, with a peak efficiency of 5.23% at 3.2 V and a roll-off efficiency of 52.77% at 7 V.

The reference OLED, without any surface modification, displayed lower peak efficiency, 4.92% at 3.6 V, but demonstrated the highest roll-off efficiency of 79.26% at 7 V, retaining much of its initial performance under higher operating voltages. Despite its lower peak efficiency, this reference OLED had the best stability across voltage increases, making it more resilient in high-voltage conditions compared with the salt-modified versions.

The inset of Figure 5e shows the lifetime measurements on metal chloride, LiF-based, and reference OLEDs. This lifetime measurement of an OLED involves evaluating how its performance changes over time under specific operating conditions. To this end, the OLEDs have operated under a constant current stress of 10 mA and were monitored overtime (72 h). The stability of the OLED is assessed by how consistently it maintains its performance metrics (like voltage) over time. LiF-based OLED demonstrates the smallest variations in voltage (29% increment in voltage after 72 h), indicating that it is more stable compared to metal chlorides. However, OLEDs based on CsCl, NaCl, and RbCl have demonstrated better stability compared to the reference device without any interfacial layer, with an increase in voltage of around 36%, which is less than the 50% increase observed in the reference sample. In addition, higher current densities for CsCl- and RbCl-based devices are observed, caused by a more balanced carrier injection and transfer to the active layer in the OLED stack. A detailed summary is given in Table S6. The luminous efficacy illustrates relatively high values for OLEDs with an interfacial layer at lower voltages, which is desirable because it indicates that the OLED is efficient in converting electricity into light at lower voltages.

Figure S17a demonstrates the EL peak intensity for different reference devices. All metal chlorides as well as LiF have been added to the OLED structure as an electron injection layer by removing the ZnO:PEIE NC to study their influence further on electron injection. First of all, from EL measurements, it is proven that metal chloride cannot be used as an individual electron injector as it will negatively affect the performance of the OLEDs. Second, all metal chloride electron injection layers show better performance than LiF. Changing the electron injection layer from Ca to ZnO:PEIE NC reported previously[31] and shown in Figure S17b leads to a better performing OLED. The addition of interfacial layers to the OLED stack with ZnO:PEIE NC improves the overall performance of the OLEDs.

4. CONCLUSIONS

In conclusion, our comprehensive investigation of the influence of metal chlorides, specifically sodium chloride (NaCl), cesium chloride (CsCl), rubidium chloride (RbCl), and potassium chloride (KCl), as alternative interfacial layers in optoelectronic devices has yielded significant scientific insights and promising practical applications, primarily in the context of organic light-emitting diodes (OLEDs).

From a scientific standpoint, our study reveals the pivotal role of interface engineering in optimizing optoelectronic device performance. By incorporating metal chloride interfacial layers, we have addressed critical challenges, including the reduction of potential energy barriers, the mitigation of interface traps, and the control of charge recombination processes. Through a range of experimental techniques, including electron paramagnetic resonance (EPR), X-ray and ultraviolet photoelectron spectroscopy (XPS/UPS), density functional theory (DFT) calculations, capacitance−voltage ($C-V$) measurements, and electrochemical impedance spectroscopy (EIS), we have unraveled the underlying mechanisms responsible for the improved performance of the OLEDs.

Our findings indicate that the integration of metal chloride layers combined with the ZnO:PEIE nanocomposite enhances charge transport through the layer because the efficiency (or dynamics) of the trapping of charges in the ZnO nanocomposite is reduced. This correlates with a close to 50% reduction of trapped charges in ZnO, as extracted from $C-V$ measurements, and thus a more efficient charge transport to the emissive layer. Additionally, from XPS/UPS experiments, the shifts in work function induced by metal chlorides acting as interface dipoles contribute to a lower energy barrier for electron injection, further enhancing the overall performance of the NaCl-based OLED. EIS and Nyquist plots provided further insights into the charge dynamics and ionic behavior within the OLED stack.

From an application perspective, the practical implications of our study are particularly evident in the field of OLEDs. The integration of RbCl, CsCl, NaCl, and KCl as interfacial layers in OLED architectures has led to a substantial reduction in the potential energy barrier between the electron injection layer (EIL) and the aluminum (Al) electrode, accompanied by significant enhancements in irradiance. These enhancements in the performance of the OLEDs include a lower turn-on voltage (almost 50% reduction by addition of the RbCl layer), a higher electroluminescence intensity (25% higher than the reference device for the RbCl-based OLED), improved current density, enhanced operational stability compared to the reference devices, and enhanced external quantum efficiency (EQE) (20% higher for NaCl-based OLED). NaCl-based OLEDs demonstrated the best stability, with a roll-off efficiency of 65.13% compared to other metal chloride-based OLEDs. The

https://doi.org/10.1021/acsami.4c16558
ACS Appl. Mater. Interfaces 2024, 16, 65687−65701

reference OLED, while having a lower peak efficiency, exhibited the highest roll-off efficiency of 79.26%, showing better performance stability under high voltage conditions and holding great promise for the development of more efficient and cost-effective optoelectronic devices.

■ ASSOCIATED CONTENT

Supporting Information

The Supporting Information is available free of charge at https://pubs.acs.org/doi/10.1021/acsami.4c16558.

Additional experimental data, methods, and characterizations; AFM images and measured height profile plots; transmission spectra; schematic structure of the proposed OLED device; Nyquist plots and equivalent circuit model; fitted curves of the capacitance versus frequency curves for the measured data; capacitance−voltage characteristics; EPR signals; normalized EPR intensity; TR-EPR results; ratio of fast and slow recombination kinetics; band structure and slab model; XPS spectra; fitting of peaks from XPS; comparison of electrical properties; EL intensity plots; summary of experimental parameters and outcomes; detailed analysis; and supplementary procedures (PDF)

■ AUTHOR INFORMATION

Corresponding Author

Wim Deferme − *Hasselt University, Institute for Materials Research (imo-imomec), B-3500 Hasselt, Belgium; imec, imo-imomec, B-3590 Diepenbeek, Belgium;* orcid.org/0000-0002-8982-959X; Email: wim.deferme@uhasselt.be

Authors

Shabnam Ahadzadeh − *Hasselt University, Institute for Materials Research (imo-imomec), B-3500 Hasselt, Belgium; imec, imo-imomec, B-3590 Diepenbeek, Belgium; Theory and Spectroscopy of Molecules and Materials (TSM²), Physics Department, University of Antwerp, Antwerp 2610, Belgium;* orcid.org/0000-0002-4863-530X

Beatriz de la Fuente − *Research Group Sustainable Materials Engineering (SUME), Lab of Electrochemical and Surface Engineering (SURF), Vrije Universiteit Brussel, Brussels 1050, Belgium;* orcid.org/0000-0001-9045-3481

Hamid Hamed − *imec, imo-imomec, B-3590 Diepenbeek, Belgium; Energy Ville, IMO-IMOMEC, Genk 3600, Belgium*

Guy Brammertz − *Hasselt University, Institute for Materials Research (imo-imomec), B-3500 Hasselt, Belgium; imec, imo-imomec, B-3590 Diepenbeek, Belgium; Energy Ville, IMO-IMOMEC, Genk 3600, Belgium*

Tom Hauffman − *Research Group Sustainable Materials Engineering (SUME), Lab of Electrochemical and Surface Engineering (SURF), Vrije Universiteit Brussel, Brussels 1050, Belgium*

Sofie Cambré − *Theory and Spectroscopy of Molecules and Materials (TSM²), Physics Department, University of Antwerp, Antwerp 2610, Belgium;* orcid.org/0000-0001-7471-7678

Rachith Shanivarasanthe Nithyananda Kumar − *Hasselt University, Institute for Materials Research (imo-imomec), B-3500 Hasselt, Belgium; imec, imo-imomec, B-3590 Diepenbeek, Belgium;* orcid.org/0000-0003-1453-4495

Complete contact information is available at: https://pubs.acs.org/10.1021/acsami.4c16558

Author Contributions

Shabnam Ahadzadeh, Rachith S. N., and Wim. Deferme conceived and designed the study; Shabnam Ahadzadeh collected and analyzed the data and wrote a first draft of the manuscript. Shabnam Ahadzadeh processed and characterized OLEDs and conducted *C*−*V*, *I*−*V*, EQE, and EL measurements and DFT calculations. Sofie Cambré and Shabnam Ahadzadeh performed the EPR measurements and their analysis. Rachith S. N. conducted the AFM measurements. Beatriz de la Fuente conducted XPS and UPS measurements supervised by Tom Hauffman. Wim Deferme, Rachith S. N., and Sofie Cambré helped with data analysis. Hamid Hamed conducted EIS measurements. The manuscript was written through contributions of all authors. All authors have given approval to the final version of the manuscript.

Funding

The authors would like to thank the fund for scientific research—Flanders (FWO) for providing S.A. with a SB PhD grant with grant numbers 1SA4523N and 1SA4525N and BOF funding from UHasselt under grant number BOF22IN-CENT09 for the present work. S.C. thanks the FWO for providing infrastructure funding for the EPR instrumentation (I004920N). The XPS used in this work has been funded by the Research Foundation—Flanders under grant number I00620N.

Notes

The authors declare no competing financial interest.

■ ACKNOWLEDGMENTS

The authors thank Prof. Dr. Anitha Ethirajan at the Institute for Materials Research (imo-imomec), UHasselt, Belgium, and Prof. Frank Renner for their support of the AFM measurements and Lennert Purnal and Dieter Reenaers at the Institute for Materials Research (imo-imomec), UHasselt, Belgium, for their support on measurement setup and software. The authors also thank scientific research—Flanders (FWO) and BOF fundings for their support.

■ ABBREVIATIONS

NP, nanoparticle; EIL, electron injection layer; MoO_3, molybdenum oxide; LiF, lithium fluoride; NaF, sodium fluoride; WF, work function; UV, ultraviolet ozone; ALD, atomic layer depositioe; PET, polyethylene terephthalate; MC, metal chloride; OLED, organic light emitting diode; NaCl, sodium chloride; CsCl, cesium chloride; RbCl, rubidium chloride; KCl, potassium chloride; EPR, electron paramagnetic resonance; XPS, X-ray photoelectron spectroscopy; UPS, ultraviolet photoelectron spectroscopy; DFT, density functional theory; PEDOT:PSS, poly(3,4-ethylenedioxythiophene) polystyrene sulfonate; SY, poly(*para*-phenylene vinylene) copolymer; ZnO:PEIE NC, zinc oxide:polyethyleneimine ethoxylated nanocomposite; EL, electroluminescence; EQE, external quantum efficiency; AFM, atomic force microscopy; ETL, electron transport layer; EML, emissive layer; HTL, hole transport layer; EIS, electrochemical impedance spectroscopy

■ REFERENCES

(1) Moun, M.; Singh, R. Metal−Semiconductor Interface Engineering in Layered 2d Materials for Device Applications. *Bull. Mater. Sci.* **2021**, *44* (3), 223.

(2) Hofmann, O. T.; Rinke, P.; Scheffler, M.; Heimel, G. Integer Versus Fractional Charge Transfer at Metal (/Insulator)/Organic Interfaces: Cu(/NaCl)/TCNE. *ACS Nano* **2015**, *9* (5), 5391−5404.

(3) Jeon, S. H.; Kang, S. Unraveling the Injection Barrier between Electrode and Organic Layer in OLED Device: A Theoretical Prediction Model. *Comput. Theor. Chem.* **2023**, *1226*, 114185.
(4) Al-Qrinawi, M. S.; El-Agez, T. M.; Abdel-Latif, M. S.; Taya, S. A. Capacitance-Voltage Measurements of Hetero-Layer OLEDs Treated by an Electric Field and Thermal Annealing. *Int. J. Thin Film Sci. Technol.* **2021**, *10*, 217−226.
(5) Wang, F.; Sun, W.; Liu, P.; Wang, Z.; Zhang, J.; Wei, J.; Li, Y.; Hayat, T.; Alsaedi, A.; Tan, Z. a. Achieving Balanced Charge Injection of Blue Quantum Dot Light-Emitting Diodes through Transport Layer Doping Strategies. *J. Phys. Chem. Lett.* **2019**, *10* (5), 960−965.
(6) Kotadiya, N. B.; Blom, P. W.; Wetzelaer, G.-J. A. Efficient and Stable Single-Layer Organic Light-Emitting Diodes Based on Thermally Activated Delayed Fluorescence. *Nat. Photonics* **2019**, *13* (11), 765−769.
(7) Tang, A.; Xiao, B.; Wang, Y.; Gao, F.; Tajima, K.; Bin, H.; Zhang, Z. G.; Li, Y.; Wei, Z.; Zhou, E. Simultaneously Achieved High Open-Circuit Voltage and Efficient Charge Generation by Fine-Tuning Charge-Transfer Driving Force in Nonfullerene Polymer Solar Cells. *Adv. Funct. Mater.* **2018**, *28* (6), 1704507.
(8) Yang, L.; Dall'Agnese, C.; Dall'Agnese, Y.; Chen, G.; Gao, Y.; Sanehira, Y.; Jena, A. K.; Wang, X. F.; Gogotsi, Y.; Miyasaka, T. Surface-Modified Metallic $Ti_3C_2T_x$ Mxene as Electron Transport Layer for Planar Heterojunction Perovskite Solar Cells. *Adv. Funct. Mater.* **2019**, *29* (46), 1905694.
(9) Ren, W.; Son, K. R.; Kim, T. G. Performance Improvement of Blue Tadf Top-Emission OLEDs by Tuning Hole Injection Barriers Using a Nickel-Doped Silicon Dioxide Buffer Layer. *Appl. Surf. Sci.* **2023**, *612*, 155948.
(10) Zhu, G.; Fan, Q.; Hu, T.; Han, Y.; Zhang, G.; Zou, J.; Tao, H.; Wang, L.; Peng, J. Largely Improving the Lifetime by Inserting a Yb Metal Layer into the Charge Generation Layer in Tandem Organic Light-Emitting Diodes. *Org. Electron.* **2023**, *122*, 106908.
(11) Zojer, E.; Taucher, T. C.; Hofmann, O. T. The Impact of Dipolar Layers on the Electronic Properties of Organic/Inorganic Hybrid Interfaces. *Adv. Mater. Interfaces* **2019**, *6* (14), 1900581.
(12) Chen, Q.; Wang, C.; Li, Y.; Chen, L. Interfacial Dipole in Organic and Perovskite Solar Cells. *J. Am. Chem. Soc.* **2020**, *142* (43), 18281−18292.
(13) Paniagua, S. A.; Hotchkiss, P. J.; Jones, S. C.; Marder, S. R.; Mudalige, A.; Marrikar, F. S.; Pemberton, J. E.; Armstrong, N. R. Phosphonic Acid Modification of Indium− Tin Oxide Electrodes: Combined XPS/UPS/Contact Angle Studies. *J. Phys. Chem. C* **2008**, *112* (21), 7809−7817.
(14) Singh, N.; Mohapatra, A.; Chu, C.-W.; Tao, Y.-T. Modulation of Work Function of Ito by Self-Assembled Monolayer and Its Effect on Device Characteristics of Inverted Perovskite Solar Cells. *Org. Electron.* **2021**, *98*, 106297.
(15) Peng, X.; Hu, L.; Qin, F.; Zhou, Y.; Chu, P. K. Low Work Function Surface Modifiers for Solution-Processed Electronics: A Review. *Adv. Mater. Interfaces* **2018**, *5* (10), 1701404.
(16) Rajendran, M. V.; Alagumalai, A.; Ganesan, S.; Menon, V. S.; Raman, R. K.; Gurusamy Thangavelu, S. A.; Krishnamoorthy, A. Design and synthesis of multifaceted dicyanomethylene rhodanine linked thiophene: a SnO_x−perovskite dual interface modifier facilitating enhanced device performance through improved Fermi level alignment, defect passivation and reduced energy loss. *Sustain. Energy Fuels* **2023**, *7* (3), 735−751.
(17) Ameen, M. Y.; Pradhan, S.; Suresh, M. R.; Reddy, V. MoO_3 Anode Buffer Layer for Efficient and Stable Small Molecular Organic Solar Cells. *Opt. Mater.* **2015**, *39*, 134−139.
(18) Brabec, C. J.; Shaheen, S. E.; Winder, C.; Sariciftci, N. S.; Denk, P. Effect of LiF/Metal Electrodes on the Performance of Plastic Solar Cells. *Appl. Phys. Lett.* **2002**, *80* (7), 1288−1290.
(19) Bishnoi, S.; Datt, R.; Arya, S.; Gupta, S.; Gupta, R.; Tsoi, W. C.; Sharma, S. N.; Patole, S. P.; Gupta, V. Engineered Cathode Buffer Layers for Highly Efficient Organic Solar Cells: A Review. *Adv. Mater. Interfaces* **2022**, *9* (19), 2101693.
(20) Turak, A. On the Role of LiF in Organic Optoelectronics. *Electron. Mater.* **2021**, *2* (2), 198−221.
(21) Qu, X.; Zhang, N.; Cai, R.; Kang, B.; Chen, S.; Xu, B.; Wang, K.; Sun, X. W. Improving Blue Quantum Dot Light-Emitting Diodes by a Lithium Fluoride Interfacial Layer. *Appl. Phys. Lett.* **2019**, *114* (7), 071101.
(22) Tan, D.; Zhang, X.; Liu, X.; Zhang, H.; Ma, D. Stability Enhancement of Inverted Perovskite Solar Cells Using LiF in Electron Transport Layer. *Org. Electron.* **2020**, *80*, 105613.
(23) Gao, F.; Luo, C.; Wang, X.; Zhao, Q. Alkali Metal Chloride-Doped Water-Based TiO_2 for Efficient and Stable Planar Perovskite Photovoltaics Exceeding 23% Efficiency. *Small Methods* **2021**, *5* (12), 2100856.
(24) Li, Z.; Li, D.; Wang, H.; Chen, P.; Pi, L.; Zhou, X.; Zhai, T. Intercalation Strategy in 2d Materials for Electronics and Optoelectronics. *Small Methods* **2021**, *5* (9), 2100567.
(25) Zou, Y.; Deng, Z.; Xu, D.; Lü, Z.; Yin, Y.; Du, H.; Chen, Z.; Wang, Y. Enhanced Brightness of Organic Light-Emitting Diodes Based on Mg: Ag Cathode Using Alkali Metal Chlorides as an Electron Injection Layer. *J. Lumin.* **2012**, *132* (2), 414−417.
(26) Earmme, T.; Jenekhe, S. A. Solution-Processed, Alkali Metal-Salt-Doped, Electron-Transport Layers for High-Performance Phosphorescent Organic Light-Emitting Diodes. *Adv. Funct. Mater.* **2012**, *22* (24), 5126−5136.
(27) Lee, D. K.; Kim, T. S.; Choi, J.-Y.; Yu, H. K. Recrystallized NaCl from Thin Film to Nano-/Microsized Sacrificial Crystal for Metal Nanostructures. *Cryst. Growth Des.* **2018**, *18* (9), 5295−5300.
(28) Shah, D.; Patel, D. I.; Roychowdhury, T.; Johnson, B. I.; Linford, M. R. Substrate Protection and Deprotection with Salt Films to Prevent Surface Contamination and Enable Selective Atomic Layer Deposition. *Appl. Surf. Sci.* **2020**, *526*, 146621.
(29) Lü, Z.; Deng, Z.; Hou, Y.; Xu, H. Similarities and Differences of Alkali Metal Chlorides Applied in Organic Light-Emitting Diodes. *Thin Solid Films* **2012**, *525*, 106−109.
(30) Lü, Z.; Wang, Y.; Zou, Y.; Du, H.; Chen, Z.; Deng, Z. The Effect of Alkaline Metal Chlorides on the Properties of Organic Light-Emitting Diodes. *J. Lumin.* **2010**, *130* (3), 387−391.
(31) Kumar, R. S. N.; Breugelmans, R.; Jiang, X.; Ahadzadeh, S.; Brammertz, G.; Verding, P.; Daenen, M.; Van Landeghem, M.; Cambré, S.; Vandewal, K. Organic-Inorganic Nanoparticle Composite as an Electron Injection/Hole Blocking Layer in Organic Light Emitting Diodes for Large Area Lighting Applications. *Appl. Surf. Sci.* **2023**, *631*, 157548.
(32) Von Hauff, E. Impedance Spectroscopy for Emerging Photovoltaics. *J. Phys. Chem. C* **2019**, *123* (18), 11329−11346.
(33) Altazin, S.; Züfle, S.; Knapp, E.; Kirsch, C.; Schmidt, T. D.; Jäger, L.; Noguchi, Y.; Brütting, W.; Ruhstaller, B. Simulation of OLEDs with a Polar Electron Transport Layer. *Org. Electron.* **2016**, *39*, 244−249.
(34) Liu, Q.; Zeiske, S.; Jiang, X.; Desta, D.; Mertens, S.; Gielen, S.; Shanivarasanthe, R.; Boyen, H.-G.; Armin, A.; Vandewal, K. Electron-Donating Amine-Interlayer Induced N-Type Doping of Polymer: Nonfullerene Blends for Efficient Narrowband near-Infrared Photodetection. *Nat. Commun.* **2022**, *13* (1), 5194.
(35) Zhang, L.; Nakanotani, H.; Adachi, C. Capacitance-Voltage Characteristics of a 4, 4′-Bis [(N-Carbazole) Styryl] Biphenyl Based Organic Light-Emitting Diode: Implications for Characteristic Times and Their Distribution. *Appl. Phys. Lett.* **2013**, *103* (9), 093301.
(36) Zhao, Y.; Lin, Y.; Zeng, Z.; Su, C.; Jiang, C. Determination of the Dynamic Dielectric Function of Pedot: PSS from the Visible to the near-Infrared Region. *Opt. Mater. Express* **2021**, *11* (9), 3049−3055.
(37) Hughes, M. P.; Rosenthal, K. D.; Ran, N. A.; Seifrid, M.; Bazan, G. C.; Nguyen, T. Q. Determining the Dielectric Constants of Organic Photovoltaic Materials Using Impedance Spectroscopy. *Adv. Funct. Mater.* **2018**, *28* (32), 1801542.
(38) Kaur, D.; Bharti, A.; Sharma, T.; Madhu, C. Dielectric Properties of ZnO-Based Nanocomposites and Their Potential Applications. *Int. J. Opt.* **2021**, *2021*, 1−20.

https://doi.org/10.1021/acsami.4c16558
ACS Appl. Mater. Interfaces 2024, 16, 65687−65701

(39) Ahmad, M. P.; Rao, A. V.; Babu, K. S.; Rao, G. N. Particle Size Effect on the Dielectric Properties of ZnO Nanoparticles. *Mater. Chem. Phys.* **2019**, *224*, 79−84.
(40) Züfle, S.; Altazin, S.; Hofmann, A.; Jäger, L.; Neukom, M. T.; Schmidt, T. D.; Brütting, W.; Ruhstaller, B. The Use of Charge Extraction by Linearly Increasing Voltage in Polar Organic Light-Emitting Diodes. *J. Appl. Phys.* **2017**, *121* (17), 175501.
(41) Qu, X.; Sun, X. Impedance Spectroscopy for Quantum Dot Light-Emitting Diodes. *J. Semicond.* **2023**, *44* (9), 091603.
(42) Züfle, S.; Altazin, S.; Hofmann, A.; Jäger, L.; Neukom, M. T.; Brütting, W.; Ruhstaller, B. Determination of Charge Transport Activation Energy and Injection Barrier in Organic Semiconductor Devices. *J. Appl. Phys.* **2017**, *122* (11), 115502.
(43) Chattopadhyay, P.; Raychaudhuri, B. Frequency Dependence of Forward Capacitance-Voltage Characteristics of Schottky Barrier Diodes. *Solid State Electron.* **1993**, *36* (4), 605−610.
(44) Ellis, C. L.; Smith, E.; Javaid, H.; Berns, G.; Venkataraman, D. Ion Migration in Hybrid Perovskites: Evolving Understanding of a Dynamic Phenomenon. In *Perovskite Photovoltaics*; Elsevier, 2018; pp 163−196.
(45) Guerrero, A.; Bisquert, J.; Garcia-Belmonte, G. Impedance Spectroscopy of Metal Halide Perovskite Solar Cells from the Perspective of Equivalent Circuits. *Chem. Rev.* **2021**, *121* (23), 14430−14484.
(46) Correa-Baena, J.-P.; Turren-Cruz, S.-H.; Tress, W.; Hagfeldt, A.; Aranda, C.; Shooshtari, L.; Bisquert, J.; Guerrero, A. Changes from Bulk to Surface Recombination Mechanisms between Pristine and Cycled Perovskite Solar Cells. *ACS Energy Lett.* **2017**, *2* (3), 681−688.
(47) Martens, H.; Pasveer, W.; Brom, H.; Huiberts, J.; Blom, P. Crossover from Space-Charge-Limited to Recombination-Limited Transport in Polymer Light-Emitting Diodes. *Phys. Rev. B: Condens. Matter Mater. Phys.* **2001**, *63* (12), 125328.
(48) Simmons, J. G. Poole-Frenkel Effect and Schottky Effect in Metal-Insulator-Metal Systems. *Phys. Rev.* **1967**, *155* (3), 657−660.
(49) Zaini, M. S.; Mohd Sarjidan, M.; Majid, W. A. The Effect of Trap Density on the Trapping and De-Trapping Processes in Determining the Turn-on Voltage of Double-Carrier Organic Light-Emitting Devices (OLEDs). *J. Electron. Mater.* **2021**, *50* (8), 4511−4523.
(50) Rezaie, M. N.; Mohammadnejad, S.; Ahadzadeh, S. Hybrid Inorganic-Organic Light-Emitting Heterostructure Devices Based on ZnO. *Opt Laser. Technol.* **2021**, *138*, 106896.
(51) Andia-Huaracha, S.; Zapana-Cayo, L.; Aragón, F. F. H.; Aquino, J. C. R.; Coaquira, J.; Gonzales-Lorenzo, C.; Ayala-Arenas, J.; Solis, J.; Morais, P.; Pacheco-Salazar, D. Tuning the Photocatalytic Activity of ZnO Nanoparticles by the Annihilation of Intrinsic Defects Provoked by the Thermal Annealing. *J. Nanopart. Res.* **2022**, *24* (3), 50.
(52) Altaf, C. T.; Coskun, O.; Kumtepe, A.; Rostas, A. M.; Iatsunskyi, I.; Coy, E.; Erdem, E.; Sankir, M.; Sankir, N. D. Photo-Supercapacitors Based on Nanoscaled ZnO. *Sci. Rep.* **2022**, *12* (1), 11487.
(53) Ke, S.-C.; Wang, T.-C.; Wong, M.-S.; Gopal, N. O. Low Temperature Kinetics and Energetics of the Electron and Hole Traps in Irradiated TiO_2 Nanoparticles as Revealed by EPR Spectroscopy. *J. Phys. Chem. B* **2006**, *110* (24), 11628−11634.
(54) Montes, E.; Vazquez, H. Calculation of Energy Level Alignment and Interface Electronic Structure in Molecular Junctions Beyond DFT. *J. Phys. Chem. C* **2021**, *125* (46), 25825−25831.
(55) Liu, M.; Jin, Y.; Pan, J. Relevance of Implicit and Explicit Solvent in Density-Functional Theory Study of Adsorption at Electrochemical NaCl/Al Interface. *Mater. Today Commun.* **2022**, *31*, 103425.
(56) Bickelhaupt, F. M.; Baerends, E. J. Kohn-Sham Density Functional Theory: Predicting and Understanding Chemistry. *Rev. Comput. Chem.* **2000**, *15*, 1−86.
(57) Camacho-Berrios, A. A.; Pantojas, V. M.; Otano, W. Reactive Sputtered ZnO Thin Films: Influence of the O_2/Ar Flow Ratio on the Oxygen Vacancies and Paramagnetic Active Sites. *Thin Solid Films* **2019**, *692*, 137641.
(58) Kadam, K. D.; Kim, H.; Rehman, S.; Patil, H.; Aziz, J.; Dongale, T. D.; Khan, M. F.; Kim, D.-k. Optimization of ZnO: Peie as an Electron Transport Layer for Flexible Organic Solar Cells. *Energy Fuels* **2021**, *35* (15), 12416−12424.
(59) Ischenko, V.; Polarz, S.; Grote, D.; Stavarache, V.; Fink, K.; Driess, M. Zinc Oxide Nanoparticles with Defects. *Adv. Funct. Mater.* **2005**, *15* (12), 1945−1954.
(60) Drouilly, C.; Krafft, J.-M.; Averseng, F.; Casale, S.; Bazer-Bachi, D.; Chizallet, C.; Lecocq, V.; Vezin, H.; Lauron-Pernot, H.; Costentin, G. ZnO Oxygen Vacancies Formation and Filling Followed by in Situ Photoluminescence and in Situ EPR. *J. Phys. Chem. C* **2012**, *116* (40), 21297−21307.
(61) Azmi, R.; Hwang, S.; Yin, W.; Kim, T.-W.; Ahn, T. K.; Jang, S.-Y. High Efficiency Low-Temperature Processed Perovskite Solar Cells Integrated with Alkali Metal Doped ZnO Electron Transport Layers. *ACS Energy Lett.* **2018**, *3* (6), 1241−1246.
(62) Choi, J.; Kim, Y.; Jo, J. W.; Kim, J.; Sun, B.; Walters, G.; García de Arquer, F. P.; Quintero-Bermudez, R.; Li, Y.; Tan, C. S.; et al. Chloride Passivation of ZnO Electrodes Improves Charge Extraction in Colloidal Quantum Dot Photovoltaics. *Adv. Mater.* **2017**, *29* (33), 1702350.

https://doi.org/10.1021/acsami.4c16558
ACS Appl. Mater. Interfaces 2024, 16, 65687−65701